

A Reinvestigation of Moving Punctured Black Holes with a New Code

Zhoujian Cao*

*Institute of Applied Mathematics, Academy of Mathematics and System Science,
Chinese Academy of Sciences, Beijing 100080, China,
Theoretical Institute for Advanced Research in Astrophysics, Academia Sinica, Taiwan,
State Key Laboratory of Scientific and Engineering Computing, China*

Hwei-Jang Yo[†] and Jui-Ping Yu

*Department of Physics, National Cheng-Kung University, Tainan 701, Taiwan
(Dated: February 12, 2022)*

We report on our code, in which the moving puncture method is applied and an adaptive/fixed mesh refinement is implemented, and on its preliminary performance on black hole simulations. Based on the BSSN formulation, up-to-date gauge conditions and the modifications of the formulation are also implemented and tested. In this work we present our primary results about the simulation of a single static black hole, of a moving single black hole, and of the head-on collision of a binary black hole system. For the static punctured black hole simulations, different modifications of the BSSN formulation are applied. It is demonstrated that both the currently used sets of modifications lead to a stable evolution. For cases of a moving punctured black hole with or without spin, we search for viable gauge conditions and study the effect of spin on the black hole evolution. Our results confirm previous results obtained by other research groups. In addition, we find a new gauge condition, which has not yet been adopted by any other researchers, which can also give stable and accurate black hole evolution calculations. We examine the performance of the code for the head-on collision of a binary black hole system, and the agreement of the gravitational waveform it produces with that obtained in other works. In order to understand qualitatively the influence of matter on the binary black hole collisions, we also investigate the same head-on collision scenarios but perturbed by a scalar field. The numerical simulations performed with this code not only give stable and accurate results that are consistent with the works by other numerical relativity groups, but also lead to the discovery of a new viable gauge condition, as well as clarify some ambiguities in the modification of the BSSN formulation. These results demonstrate that this code is reliable and ready to be used in the study of more realistic astrophysical scenarios and of numerical relativity.

PACS numbers: 04.25.Dm, 04.30.Db, 95.30.Sf, 97.60.Lf

I. INTRODUCTION

There are two main purposes for studying numerical relativity: One is to investigate the mathematical issues of the geometry of the Einstein manifold. These issues include cosmic censorship, the hoop conjecture, the Penrose inequality, and critical phenomenon [1]. The other, more practical one, is to study the dynamics of astrophysically compact objects. To meet the needs of existing (e.g., LIGO [2], VIRGO [3], GEO600 [4], and TAMA [5]) and planned (e.g. LISA [6]) gravitational wave detectors, the theoretical prediction of the gravitational waveform for realistic sources has become urgent. In both of the aspects of numerical relativity, the most important targets for study are black holes and neutron stars, especially those in binary systems.

After decades of exploration by many researchers, recently there have been exciting breakthroughs in the simulation of the evolution of binary black holes (BBHs) [7, 8, 9]. Soon after these breakthroughs, the moving

puncture method based on the BSSN formalism [10] was widely used by numerical relativity groups to deal with black hole systems [11, 12, 13] and neutron star systems [14]. Much interesting physics related to BBHs has been explored, including the waveform of the gravitational radiation [15, 16], the spin-orbit coupling effect [17], and the recoil velocity [18, 19]. It has been emphasized in almost all of these studies that the treatment of the singularity problem, i.e., the moving puncture method and the gauge condition, are both key factors in this series of successes. Not needing any inner boundary condition makes the moving puncture method much simpler to handle, compared with the excision method [20]. This simplicity has made the moving puncture method popular in the numerical relativity community. The Bona-Masso type slicing gauge conditions [21] for the lapse function and many driver gauge conditions (e.g., the Γ -driver) for the shift vector [22, 23] have been shown to be very important in making the moving puncture method work. However, in [22] it was shown that, although the details of the gauge conditions used in the punctured BBH evolutions are different, only certain gauge choices allow one to evolve a single moving puncture black hole. It is desirable to better understand the effect of the gauge choices on black hole evolutions.

*zjcao@amt.ac.cn

[†]hjyo@phys.ncku.edu.tw

In order to study numerical relativity and also investigate the specific aforementioned topics we develop, from scratch, a code based on the moving puncture method. We adopt a fourth-order finite differencing scheme for the spatial derivatives and the Crank-Nicholson scheme for the time integrations. We use the GrACE package [24] to implement both the mesh refinement and the parallelization in our code. In this paper we present our primary results about the evolution of a single static black hole, of a single moving black hole, of the head-on collision of a BBH, and of the head-on collision perturbed by a scalar field. Our results confirm many results obtained in the previous works by other groups. On the other hand we find a new gauge condition, which has not been tried by other researchers, that can also give stable and accurate black hole evolution calculations. We also observe the effects of the existence of a massless scalar field in delaying the head-on collision, depending on the initial configuration of the scalar field. All of these results enhance our confidence in this code, and thus we will apply the code to more realistic astrophysical calculations in the near future.

The remainder of the paper is organized as follows: In Section II, we first summarize the BSSN formulation, the conventional modifications and adjustments, and the gauge conditions. Then we describe the numerical methods used in this code in section III, including the details of the FMR/AMR algorithm, the finite-differencing stencils, and the Kreiss-Oliger dissipation. In Section IV, the initial data is outlined. In Section V, we present our numerical results on the evolutions of a single static black hole, of a single moving black hole with and without spin, and of the head-on collision of a BBH, with and without a massless scalar field. We summarize and discuss the implications of our findings in Sec. VI.

II. FORMULATION

A. Review of the Basic Equations

The code is based on the BSSN formalism [10], which is a conformal-traceless “3+1” formulation of the Einstein equations. In this formalism, the spacetime is decomposed into three-dimensional spacelike slices, described by a three-metric γ_{ij} ; its embedding in the four-dimensional spacetime is specified by the extrinsic curvature K_{ij} and the variables, the lapse α and shift vector β^i , that specify a coordinate system. Our conventions are that Latin indices run over 1, 2, 3, whereas Greek indices run over 0, 1, 2, 3. Throughout the paper we adopt geometrical units with $G = c = 1$. In this paper we follow the notations of [25]. The metric γ_{ij} is conformally transformed via

$$\phi \equiv \frac{1}{12} \ln \gamma, \quad \tilde{\gamma}_{ij} \equiv e^{-4\phi} \gamma_{ij}, \quad (1)$$

where γ denotes the determinant of the metric γ_{ij} . The conformal exponent ϕ is evolved as an independent variable, whereas $\tilde{\gamma}_{ij}$ is subjected to the constraint that the determinant of $\tilde{\gamma}_{ij}$ is chosen to be unimodular, i.e., $\tilde{\gamma} = 1$. The extrinsic curvature is subjected to the same conformal transformation, and its trace K is evolved as an independent variable. That is, in place of K_{ij} we evolve:

$$K \equiv \gamma^{ij} K_{ij}, \quad \tilde{A}_{ij} \equiv e^{-4\phi} K_{ij} - \frac{1}{3} \tilde{\gamma}_{ij} K. \quad (2)$$

Similar to the conformal metric, \tilde{A}_{ij} is subjected to a constraint that \tilde{A}_{ij} is traceless, i.e., $\text{tr} \tilde{A}_{ij} = 0$. New evolution variables, i.e., the conformal connections,

$$\tilde{\Gamma}^i \equiv -\tilde{\gamma}^{ij}{}_{,j}, \quad (3)$$

are introduced, defined in terms of the contraction of the spatial derivative of the inverse conformal three-metric $\tilde{\gamma}^{ij}$.

With these dynamical variables the evolution equations read

$$\partial_t \phi = \beta^i \phi_{,i} - \frac{1}{6} \alpha K + \frac{1}{6} \beta^i{}_{,i}, \quad (4)$$

$$\partial_t \tilde{\gamma}_{ij} = \beta^k \tilde{\gamma}_{ij,k} - 2\alpha \tilde{A}_{ij} + 2\tilde{\gamma}_{k(i} \beta^k{}_{,j)} - \frac{2}{3} \tilde{\gamma}_{ij} \beta^k{}_{,k}, \quad (5)$$

$$\partial_t K = \beta^i K_{,i} - D^2 \alpha + \alpha [\tilde{A}_{ij} \tilde{A}^{ij} + \frac{1}{3} K^2 + 4\pi(\rho + s)], \quad (6)$$

$$\begin{aligned} \partial_t \tilde{A}_{ij} &= \beta^k \tilde{A}_{ij,k} + e^{-4\phi} [\alpha (R_{ij} - 8\pi s_{ij}) - D_i D_j \alpha]^{TF} \\ &+ \alpha (K \tilde{A}_{ij} - 2\tilde{A}_{ik} \tilde{A}_j{}^k) + 2\tilde{A}_{k(i} \beta^k{}_{,j)} - \frac{2}{3} \tilde{A}_{ij} \beta^k{}_{,k}, \end{aligned} \quad (7)$$

$$\begin{aligned} \partial_t \tilde{\Gamma}^i &= \beta^j \tilde{\Gamma}^i{}_{,j} - 2\tilde{A}^{ij} \alpha_{,j} \\ &+ 2\alpha \left(\tilde{\Gamma}_{jk}^i \tilde{A}^{kj} - \frac{2}{3} \tilde{\gamma}^{ij} K_{,j} - 8\pi \tilde{\gamma}^{ij} s_j + 6\tilde{A}^{ij} \phi_{,j} \right) \\ &- \tilde{\Gamma}^j \beta^i{}_{,j} + \frac{2}{3} \tilde{\Gamma}^i \beta^j{}_{,j} + \frac{1}{3} \tilde{\gamma}^{ki} \beta^j{}_{,jk} + \tilde{\gamma}^{kj} \beta^i{}_{,kj}. \end{aligned} \quad (8)$$

Here ρ , s , s_i , s_{ij} are source terms which come from matter. For a vacuum spacetime $\rho = s = s_i = s_{ij} = 0$. In the above evolution equations D_i is the covariant derivative associated with the three-metric γ_{ij} , and “TF” indicates the trace-free part of tensor objects. The Ricci tensor R_{ij} is given as

$$R_{ij} = \tilde{R}_{ij} + R_{ij}^\phi, \quad (9)$$

$$\begin{aligned} \tilde{R}_{ij} &= -\frac{1}{2} \tilde{\gamma}^{mn} \tilde{\gamma}_{ij,mn} + \tilde{\gamma}_{k(i} \tilde{\Gamma}^k{}_{,j)} + \tilde{\Gamma}^k \tilde{\Gamma}_{(ij)k} \\ &+ \tilde{\gamma}^{mn} (2\tilde{\Gamma}^k{}_{m(i} \tilde{\Gamma}_{j)kn} + \tilde{\Gamma}^k{}_{in} \tilde{\Gamma}_{kmj}), \end{aligned} \quad (10)$$

$$\begin{aligned} R_{ij}^\phi &= -2\tilde{D}_i \tilde{D}_j \phi - 2\tilde{\gamma}_{ij} \tilde{D}^k \tilde{D}_k \phi \\ &+ 4\tilde{D}_i \phi \tilde{D}_j \phi - 4\tilde{\gamma}_{ij} \tilde{D}^k \phi \tilde{D}_k \phi. \end{aligned} \quad (11)$$

The Einstein equations also lead to a set of physical constraint equations that are satisfied within each spacelike

slice:

$$e^{-4\phi}(\tilde{R} - 8\tilde{D}^i\tilde{D}_i\phi - 8\tilde{D}^k\phi\tilde{D}_k\phi) + \frac{2}{3}K^2 - \tilde{A}_{ij}\tilde{A}^{ij} - 16\pi\rho = 0, \quad (12)$$

$$\tilde{D}^i\tilde{A}_{ij} + 6\tilde{A}_{ij}\tilde{D}^i\phi - \frac{2}{3}\tilde{D}_jK - 8\pi s_j = 0, \quad (13)$$

which are usually referred to as the Hamiltonian and the momentum constraints. Here $\tilde{R} = \tilde{R}^i_i$ is the conformal Ricci scalar on a three-dimensional time slice, and \tilde{D}_i is the covariant derivative associated with the conformal three-metric $\tilde{\gamma}_{ij}$. Besides being used to obtain the evolution equations (6) and (8) in the BSSN formulation, the Hamiltonian and the momentum constraints are also applied to the volume integrals of the ADM mass and the angular momentum, respectively [26]:

$$M = \frac{1}{16\pi} \oint_{\partial\Omega} (\tilde{\Gamma}^i - 8\tilde{\gamma}^{ij}\partial_j e^\phi) d\tilde{\Sigma}_i \quad (14)$$

$$= \frac{1}{16\pi} \int_{\Omega} d^3x [e^{5\phi} (16\pi\rho + \tilde{A}_{ij}\tilde{A}^{ij} - \frac{2}{3}K^2) + \tilde{\Gamma}^k_{,k} - e^\phi\tilde{R}], \quad (15)$$

$$J_i = \frac{1}{8\pi} \epsilon_{ij}{}^k \oint_{\partial\Omega} e^{6\phi} x^j \tilde{A}^{\ell k} d\tilde{\Sigma}_\ell \quad (16)$$

$$= \frac{1}{8\pi} \epsilon_{ij}{}^k \int_{\Omega} d^3x [e^{6\phi} (\tilde{A}^j_k + \frac{2}{3}x^j K_{,k} - \frac{1}{2}x^j \tilde{A}_{\ell m} \tilde{\gamma}^{\ell m}_{,k} + 8\pi x^j s_k)], \quad (17)$$

where $d\tilde{\Sigma}_i = (1/2)\epsilon_{ijk} dx^j dx^k$. These two global quantities are useful tools for the system diagnostics to validate the calculations. The volume integral (15) is slightly different from the one in [26] due to the further application of the unimodular determinant of the conformal metric (18). Refer to Appendix C for the details.

B. Equation Adjustments

The specific choice of evolution variables introduces five additional constraints,

$$\tilde{\gamma} - 1 = 0, \quad (18)$$

$$\text{tr}\tilde{A}_{ij} = 0, \quad (19)$$

$$\tilde{\Gamma}^i + \tilde{\gamma}^{ij}_{,j} = 0. \quad (20)$$

Our code actively enforces the algebraic constraints (18) and (19) by replacing $\tilde{\gamma}_{ij}$ and \tilde{A}_{ij} with the following:

$$\tilde{\gamma}_{ij} \rightarrow \tilde{\gamma}^{-1/3} \tilde{\gamma}_{ij}, \quad (21)$$

$$\tilde{A}_{ij} \rightarrow \tilde{A}_{ij} - \frac{1}{3} \tilde{\gamma}_{ij} \text{tr}\tilde{A}_{ij}. \quad (22)$$

To enforce Eq. (20) all the undifferentiated $\tilde{\Gamma}^i$ in the evolution equations are substituted with $-\tilde{\gamma}^{ij}_{,j}$.

As to the variable choice for the conformal factor, the alternative χ , first proposed in [8], has been widely adopted. In the χ method the conformal exponent ϕ [which is $O(\ln r)$ near the puncture] is replaced with a new variable $\chi \equiv e^{-4\phi}$ [which is $O(r^4)$ near the puncture]. χ grows linearly near the puncture during the time evolution; such linear behavior leads to a more accurate evolution near the puncture. In the χ method, equation (4) is replaced by

$$\partial_t \chi = \frac{2}{3} \chi (\alpha K - \beta^i_{,i}) + \beta^i \chi_{,i}. \quad (23)$$

Note that $\phi_{,i} = -\chi_{,i}/4\chi$ and $\phi_{,ij} = \chi_{,i}\chi_{,j}/4\chi^2 - \chi_{,ij}/4\chi$ are applied to the evolution equations (6), (7) [via Eq. (11)], and (8). In these substitutions, the divisions by χ need to be taken care of in the numerical implementation to avoid division by zero or unphysically negative values of χ . In [27] a small ϵ is set to replace χ in division if χ is less than ϵ . In [28] $W \equiv e^{-2\phi}$ is chosen to be the conformal factor variable instead of χ , to avoid the effect of unphysical negative values of χ on the evolution of the other variables [53]. However, we did not encounter any such difficulty in the work for this paper, therefore it is not necessary to apply the aforementioned modifications, although we anticipate the appearance of this difficulty in some complicated scenarios in future work.

C. Gauge Conditions

As mentioned in the introduction, the gauge conditions are important for the numerical simulations of dynamical spacetime, and this is especially true for the moving puncture method. The Bona-Masso type slicing gauge conditions [21] for the lapse function and many driver gauge conditions (e.g., the Γ -driver) for the shift vector [22, 23] are currently the main type of gauge conditions used in the punctured black hole calculations. In this work, we will only focus on these types of gauge conditions, which can be written as

$$\partial_t \alpha = -2\alpha K + \lambda_1 \beta^i \alpha_{,i}, \quad (24)$$

$$\partial_t \beta^i = \frac{3}{4} f(\alpha) B^i + \lambda_2 \beta^j \beta^i_{,j}, \quad (25)$$

$$\partial_t B^i = \partial_t \tilde{\Gamma}^i - \eta B^i + \lambda_3 \beta^j B^i_{,j} - \lambda_4 \beta^j \tilde{\Gamma}^i_{,j}, \quad (26)$$

where η and the four λ 's are the parameters to be chosen, and $f(\alpha)$ is a function of α . Here the λ 's can only be set to be 0 or 1. We set $f(\alpha) = 1$ in all the cases except in Sec. V A, where $f(\alpha) = \alpha$. The gauge conditions used for moving black holes in the literature include: (1) $\lambda_1 = 1, \lambda_2 = \lambda_3 = \lambda_4 = 0$ (e.g., see [19]); and (2) $\lambda_1 = \lambda_2 = \lambda_3 = \lambda_4 = 1$ (e.g., see [11, 16]), with the proper η 's. In [22], the authors investigated several cases of the above gauge equations. In [37], the authors discussed the above case (2) analytically. In this work, we will explore this problem more thoroughly (see the following sections for details). In particular, we are concerned about the effect

of the advection terms on the stability and accuracy of the evolution, and we try to find the viable gauges for moving and/or spinning black holes. Throughout this paper we will fix $\eta = 2$.

III. NUMERICAL METHOD

In this section, we briefly describe the key numerical techniques used in this work. For the discretization, our code uses the cell-centered method, which takes the data to be defined at the center of the spatial grid cell. We also use a finite centered-differencing method with fourth-order accuracy to approximate the spatial derivatives, which closely follows [29]. In the temporal part, we use the iterative Crank-Nicholson method for time integration, which gives a second-order accuracy [30]. We take $dt = (\text{Courant factor}) \times dx$, and the Courant factor is set to be $1/4$.

We apply the standard centered finite differencing approximation to all spatial derivatives except the advection terms (i.e., the terms of the form $\beta^j \partial_j F$). For these advection terms we use the following fourth-order lopsided stencils:

$$\partial_x F_{i,j,k} = \frac{1}{12dx} (-F_{i-3,j,k} + 6F_{i-2,j,k} - 18F_{i-1,j,k} + 10F_{i,j,k} + 3F_{i+1,j,k}) \quad \text{for } \beta^x < 0, \quad (27)$$

$$\partial_x F_{i,j,k} = \frac{1}{12dx} (F_{i+3,j,k} - 6F_{i+2,j,k} + 18F_{i+1,j,k} - 10F_{i,j,k} - 3F_{i-1,j,k}) \quad \text{for } \beta^x > 0, \quad (28)$$

along the x -direction. The stencils are similar along the y - and z -directions. We also install in the code a Kreiss-Oliger dissipation [31] of the form

$$\partial_t F \rightarrow \text{RHS} + \epsilon (-1)^{n/2} \sum h_i^{n+1} D_{i+}^{n/2+1} D_{i-}^{n/2+1} F, \quad (29)$$

where RHS represents the corresponding evolution equation for F , h_i is the grid spacing in the i th direction, D_{i+} and D_{i-} are the forward and backward differencing operators in the i th-direction, n is the order of the finite difference used to evaluate the RHS, and ϵ is the dissipation coefficient to be chosen in various cases.

In order to increase the numerical resolution without increasing the computation cost much, the mesh refinement method is used in the numerical simulations. We use the GrACE package [24] to implement both the mesh refinement and the parallelization in our code. This package is able to deal with the adaptive system, considering both partitioning and load-balancing for distributed adaptive mesh refinement applications. However, we only use fixed mesh refinement (FMR) in this work. The computational domain is represented by a hierarchy of nested Cartesian grids; we adopt the cell-centered scheme, and the grid hierarchy follows the Berger and Oliger algorithm [32]. The hierarchy consists of L levels of refinement indexed by $\ell = 0, \dots, L-1$, for which $\ell = 0$ is

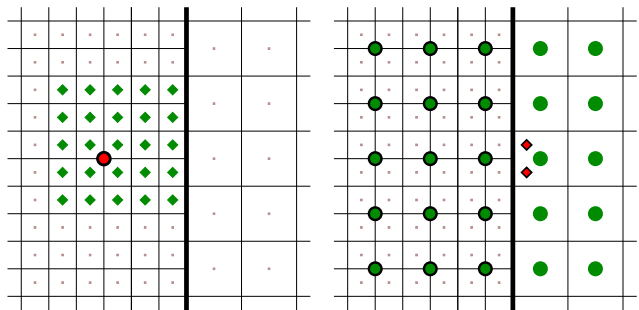


FIG. 1: (closely follows Fig.1 of [33]) Two-dimensional diagrams for the guard cell filling. The thick vertical lines in both panels represent the refinement boundaries separating fine and coarse grid regions. The left panel shows the first step, in which one of the coarse grid cells (red circles with black rim) are filled using a quartic interpolation across 25 interior fine grid cells (green diamonds). The right panel shows the second step in which two fine grid guard cells (red diamonds with black rim) are filled using quartic interpolations across 25 coarse grid values (circles). These coarse grid values include two layers of guard cells (green circles), obtained from the coarse grid region to the right of the interface, and three layers of interior cells (green circles with black rims). The final step (not shown in the figure) is to use “derivative matching” to fill the guard cells for the coarse grid.

the coarsest level and $\ell = L - 1$ is the finest one. A refinement level consists of one or more Cartesian grids with constant grid spacing h_ℓ on level ℓ . All grid blocks have the same logical structure, and refinements are bisected in each coordinate direction. A refinement factor of 2 is used such that $h_\ell = h_0/2^\ell$. The grids are properly nested such that the coordinate extent of any grid at level ℓ , $\ell > 0$, is completely covered by the grids at level $\ell - 1$. We do not refine the time step. So the time step for each level is set as $dt = (\text{Courant factor}) \times h_{\min}$, where h_{\min} is the resolution of the finest level. Therefore, there is no interpolation of data between different time slices.

Another problem in the process of the mesh refinement is how to treat the refinement boundary well to avoid possible numerical noise. Here we follow the guard cell scheme described in [33]. This method has three steps, shown in Fig. 1. In the first step, interior fine grid cells are used to fill the interior grid cells of the next lower level. This restriction operation is depicted for the case of two spatial dimensions in the left panel of Fig. 1. The restriction is basically a three-dimensional interpolation in this work, and is accurate to fourth-order in the grid spacing to match the accuracy of the finite-differencing scheme. As in the left panel of Fig. 1, the values of the coarser grid cells (red circle with black rim) located within the finer grid cells (green diamonds) are filled with the finer values by quartic interpolations. The stencil of the finer cells needs to take care to ensure that only interior fine grid points, and no fine grid guard cells, are used in this first step. Secondly, the fine grid guard cells (red diamonds with black rims) are filled by pro-

longation from the grid of the next lower level. Before the prolongation, the coarser grid updates its own cells (green circles with black rim in the right panel of Fig. 1) from the finer grids in the first step. The stencil used in the prolongation operation is shown in the right panel of Fig. 1. The prolongation is a three-dimensional interpolation, and is also accurate to fourth-order, like the restriction in the first step. In this case, the coarser grid stencil includes two layers of guard cells (green circles), as well as its updated interior grid points (green circles with black rims). In the last step, the coarser guard cells close to the interface (bold line) are filled by using derivative matching, the difference between the finer cell and the neighbor finer guard cell across the interface matches the difference between the coarser cell and the neighbor coarser cell across the interface [54].

IV. INITIAL DATA FOR PUNCTURED BLACK HOLES

For the initial data of punctured black holes, we consider the Bowen-York type initial data, in which the maximal slicing and the conformal flat form are adopted [34]. Let ψ be the conformal factor, $\psi \equiv e^\phi$. The conformal extrinsic curvature reads

$$\begin{aligned} \tilde{A}_{ij} = \psi^{-6} \hat{K}_{ij} = & \frac{3}{2} \sum_I \frac{\psi^{-6}}{r_I^2} [2P_{(i}^I n_{j)}^I \\ & - (f_{ij} - n_i^I n_j^I) P_I^k n_k^I + \frac{4}{r_I} n_{(i}^I \epsilon_{j)k\ell} S_I^k n_\ell^I], \end{aligned} \quad (30)$$

where f_{ij} is the three flat metric; P_I^i and S_I^i are constant vectors, standing for the linear momentum and spin momentum of the I -th black hole respectively; n_I^i is the radial normal vector with respect to f_{ij} , which points from the position of the I -th black hole to the space point. In the puncture method described in [34], $\psi = 1 + \sum \frac{m_I}{2r_I} + u$ with mass parameter m_I for the I -th black hole, and u is determined by

$$(\partial_x^2 + \partial_y^2 + \partial_z^2)u = -\frac{1}{8} \hat{K}^{ij} \hat{K}_{ij} (1 + \sum_I \frac{m_I}{2r_I} + u)^{-7}. \quad (31)$$

If all black holes are at rest and spinless, (30) implies $\hat{K}_{ij} = 0$, so $u = 0$. In the head-on collision case, we will implement this kind of initial data with $m_1 = m_2 = 0.5$. For a single black hole, when the linear momentum and the spin are small, we can solve the above equation approximately as (see Appendix A for more detail) [35]

$$\begin{aligned} u = \frac{\vec{P}^2}{m^2} [u_1 + u_2(3\mu_P^2 - 1)] + \frac{6u_3}{m^4} \vec{S}^2 (1 + \mu_S^2) \\ + \frac{u_4}{m^3} \vec{P} \times \vec{S} \cdot \vec{n}, \end{aligned} \quad (32)$$

with

$$\begin{aligned} u_1 &= \frac{5\ell}{8} (1 - 2\ell + 2\ell^2 - \ell^3 + \frac{1}{5}\ell^4), \\ u_2 &= \frac{1}{40b^2} (15 + 117\ell - 79\ell^2 + 43\ell^3 \\ &\quad - 14\ell^4 + 2\ell^5 + 84 \ln \ell/b), \\ u_3 &= \frac{\ell}{20} (1 + \ell + \ell^2 - 4\ell^3 + 2\ell^4), \\ u_4 &= \frac{\ell^2}{10} (10 - 25\ell + 21\ell^2 - 6\ell^3), \end{aligned} \quad (33)$$

where $b = 2r/m$, $\ell = 1/(1+b)$, $\mu_P = \vec{P} \cdot \vec{n}/P$ and $\mu_S = \vec{S} \cdot \vec{n}/S$. For the approximate solution (32) of a moving black hole with spin, the ADM mass, the linear momentum, and the angular momentum are

$$M_{\text{ADM}} = m + \frac{5}{8} \frac{\vec{P}^2}{m} + \frac{2}{5} \frac{\vec{S}^2}{m^3}, \quad (34)$$

$$\vec{P}_{\text{ADM}} = \vec{P}, \quad (35)$$

$$\vec{S}_{\text{ADM}} = \vec{S}. \quad (36)$$

On the other hand, when $\vec{P} = 0$ while \vec{S} is very large, the conformal factor can be approximated as (see Appendix A for more detail) [36]

$$\psi = \frac{(6S^2)^{1/8}}{\sqrt{r}}. \quad (37)$$

In this paper we will fix $m = 1$ for all single black hole simulations.

V. NUMERICAL RESULTS

In this section we report the numerical results for: (1) a single moving black hole without and with spin: The moving action and the spinning action of a single black hole are fundamental elements for BBH simulations. As our code aims at simulating BBH coalescence, evolving a single moving and spinning black hole becomes an essential test. In addition, since the gauge choice is critical for the moving puncture method, we would like to study if there are any other gauge conditions which can also support the moving puncture technique, besides the known ones. Our main achievement in this part of the work is that we discover one new gauge condition besides the known ones which can support moving puncture black hole simulations. The results on the gauge condition tests are listed in Table I, where Gauge VII is the aforementioned new set of gauge conditions. The successes of the gauge usage in other groups' work, e.g., [8, 9, 11, 12, 13, 22], are also reconfirmed in Table I. (2) the head-on collisions of BBHs: The head-on collision of a BBH system is the simplest dynamical spacetime in which a complete gravitational waveform of the merger of two black holes could be produced. Therefore, we use

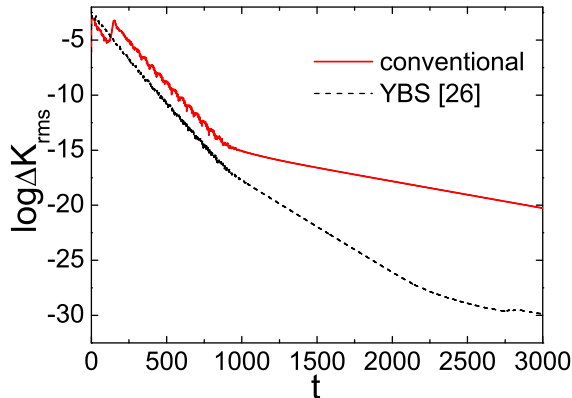


FIG. 2: The root mean square of the change in the trace of extrinsic curvature between consecutive time steps as a function of time in the static case with equatorial symmetry. The solid (red) line is the result with the conventional setting. The dashed line is the result with the modifications suggested in [26]. This shows that the both settings give stable and convergent results.

this scenario to examine the performance of the code. Besides, in order to go beyond the cases of a head-on collision in vacuum, the case of a head-on collision perturbed by a massless scalar field is also studied. With such kinds of cases we try to understand qualitatively the effect of the existence of neutral matter on the collision of a BBH, especially on its gravitational radiation. It is shown that the waveform could be affected significantly by the scalar field.

A. Static Black Hole

Although the BSSN formulation with the “1+log” lapse condition and the Γ -driver shift condition has been shown to be well-posed and hyperbolic [37, 38], it is still useful to confirm the stability and convergence of the formulation and the applied modifications before we move forwards to the moving/spinning black hole cases in the following subsections. Therefore, for the equation adjustments, we enforce the constraints (18)–(20) by using Eqs. (21) and (22), and the substitution of the conformal connection $\tilde{\Gamma}^i$ with $-\tilde{\gamma}^{ij}{}_{,j}$, as described in Sec. II B. For the gauge condition, Eqs. (24)–(26) are applied with $f(\alpha) = \alpha$ and the parameter choice $\lambda_3 = 0$, $\lambda_1 = \lambda_2 = \lambda_4 = 1$, which is close to Gauge VII in Table I, i.e., the newly viable gauge condition (see Section V B). The grid width $h = 0.2$ and the outer boundary is $\pm 16, \pm 16, 16$, respectively, assuming equatorial symmetry. In this simple case we only consider a unigrid for the computational domain.

The result for such a conventional setting is shown in

TABLE I: The gauge choices tested in this work correspond to Eqs. (24), (25) and (26); “ \checkmark ” stands for the gauge condition with the corresponding advection term, while “ \times ” stands for without.

Gauge No.	$\beta^i \partial_i \alpha$	$\beta^j \partial_j \beta^i$	$\beta^j \partial_j B^i$	$\beta^j \partial_j \tilde{\Gamma}^i$	Tests
I	\times	\times	\times	\times	FAIL
II	\checkmark	\times	\times	\times	PASS
III	\checkmark	\checkmark	\times	\times	FAIL
IV	\checkmark	\times	\checkmark	\times	FAIL
V	\checkmark	\times	\times	\checkmark	FAIL
VI	\checkmark	\checkmark	\checkmark	\times	FAIL
VII	\checkmark	\checkmark	\times	\checkmark	PASS
VIII	\checkmark	\times	\checkmark	\checkmark	FAIL
IX	\checkmark	\checkmark	\checkmark	\checkmark	PASS

Fig. 2. This figure shows a log plot for the root mean square (r.m.s.) of the changes in the trace of extrinsic curvature K (the solid red line) between consecutive time steps. In the plot the curve of the change in K rises around $t = 200$ during the period of settlement. The change in K decreases exponentially afterwards, without a sign of rise to the end of the run. This indicates that the conventional settings give a stable evolution for a single static black hole. The result is also consistent with the analytic understanding of the BSSN formulation and of the gauge choice.

Meanwhile, some modifications [26], especially the enforcement of the constraints (18)–(20), have been shown to be at least as good as the conventional ones in the numerical result [13]. We are therefore interested in understanding the performance of the code with the modifications, and the comparison between these two sets.

Briefly, the modifications in [26] are summarized as follows: Instead of treating all components of $\tilde{\gamma}_{ij}$ equally, only five of the six components of $\tilde{\gamma}_{ij}$ are evolved dynamically, and the zz -component is computed using Eq. (18),

$$\tilde{\gamma}_{zz} = 1 + \frac{\tilde{\gamma}_{yy}\tilde{\gamma}_{xz}^2 - \tilde{\gamma}_{xy}\tilde{\gamma}_{yz}\tilde{\gamma}_{xz} + \tilde{\gamma}_{xx}\tilde{\gamma}_{yz}^2}{\tilde{\gamma}_{xx}\tilde{\gamma}_{yy} - \tilde{\gamma}_{xy}^2}. \quad (38)$$

Similarly, \tilde{A}_{zz} is determined from the other five components of \tilde{A}_{ij} using Eq. (19),

$$\tilde{A}_{zz} = -\frac{\tilde{A}_x^x + \tilde{A}_y^y + \tilde{A}_{xz}\tilde{\gamma}^{xz} + \tilde{A}_{yz}\tilde{\gamma}^{yz}}{\tilde{\gamma}^{zz}}. \quad (39)$$

Instead of substituting for the undifferentiated conformal connection $\tilde{\Gamma}^i$ by $-\tilde{\gamma}^{ij}{}_{,j}$ according to the constraint (20), the constraint is added to the evolution equation (8) of $\tilde{\Gamma}^i$ via

$$\partial_t \tilde{\Gamma}^i = \text{rhs of (8)} - (\xi + 2/3)(\tilde{\Gamma}^i + \tilde{\gamma}^{ij}{}_{,j})\beta^k{}_{,k}, \quad (40)$$

where ξ is usually chosen to be $2/3$.

With otherwise the same settings as in the conventional ones, the result with the modifications in [26] is also indicated by the dashed line in Fig. 2. Without too

long a settlement period, the change in K decreases exponentially to the end of the run. A comparison of these two sets of modifications shows that they are equally good in converging the evolution to a numerically stable state, although the modifications in [26] give a better settlement at the early stage of the evolution. This indicates that there is still room for modifying the BSSN formulation to achieve better stability and convergence. The major purpose of this work is to build a reliable code for BBH simulations, therefore we will stick to the conventional modifications in the rest of this paper, although the modifications in [26] might show some subtle advantage in stabilization over the conventional ones.

B. Moving Black Hole without Spin

We now study the cases of a moving black hole without spin, which are similar to the ones in [22]. Three levels of grids are used in this and the next two subsections. The outer boundary of the coarsest level is set at ± 16 , and the boundaries of the finer levels are located at ± 8 and ± 4 , respectively. The gridwidth for the highest level is $1/8$. The black hole is located at $(0, 0, -3)$ initially with the linear momentum vector $\vec{P} = (0, 0, 1)$. The gauge choices tested in this work are listed in Table I. Gauges I, II, IV, V, VI and IX (Figs. 3, 5, 7, 8, 6, 10 in [22], respectively) have been tested in [22]. Differing from the numerical initial data used in [22], the approximate analytic initial data described in Sec. IV is used in the tests. Nevertheless, our results are consistent with the results in [22].

We summarize our results obtained for the nine tested gauges in Fig. 3. In each panel of Fig. 3, the number on the upper-right corner indicates the case with the same gauge number in Table I, and the result of that case is plotted in the panel. In each case, the black hole moves along the z -axis, and the conformal connection z -component $\tilde{\Gamma}^z$ (the red solid line), the lapse function α (the dashed line), the conformal exponent ϕ (the magenta dot-dashed line), and the shift vector z -component β^z (the blue dot-dot-dashed line) are chosen as the monitors for the stability of each run. The profiles of these variables are recorded at time $t = 30$ in each panel, except for Panel VI, where the recorded time is $t = 12$. In Panel I, it can be seen that α , ϕ , and β^z all behave well, but $\tilde{\Gamma}^z$ has some tail of ripple behind the black hole. The ripple implies a rising instability in the evolution. It is known that adding the α advection term in Eq. (24), i.e., $\lambda_1 = 1$, suppresses this unstable mode. We verify it by comparing the profiles of the variables in Panel I and II. In Panel II, all variables behave well and there is no ripple of noise for the curve of $\tilde{\Gamma}^z$. This result is consistent with the one in [39]. We then set $\lambda_1 = 1$ in Eq. (24) in the following cases, since it is necessary for the stability of a moving black hole.

In Panel III, it is shown that the addition of the advection term of $\vec{\beta}$ in Eq. (25), i.e., $\lambda_1 = \lambda_2 = 1$, will result

in a big bump behind the black hole. This instability is somehow strong, such that it causes the ill-behavior of α and ϕ . Adding the advection term of \vec{B} in Eq. (26), i.e., $\lambda_1 = \lambda_3 = 1$, will bring in a small tail, as seen in Panel IV, although such an instability does not seemingly affect α , ϕ , and β^z , for they behave well in the plot. The subtraction of the advection term of $\tilde{\Gamma}^i$ in Eq. (26), i.e., $\lambda_1 = \lambda_4 = 1$, will result in a ‘‘distorted’’ profile for $\tilde{\Gamma}^z$ in Panel V. (A gauge choice close to Gauge V has been used to simulate the inspiral of a BBH system with a small initial separation in [9].) From the above three cases, we see that solely adding the advection term of $\vec{\beta}$ or \vec{B} , or subtracting the advection term of $\tilde{\Gamma}^i$ will bring in instability in general. This understanding leads us to try combinations of these three cases.

Panel VI shows that the combination of the $\vec{\beta}$ and the \vec{B} advection term additions, i.e., $\lambda_1 = \lambda_2 = \lambda_3 = 1$, results in a profile with high frequency noise for $\tilde{\Gamma}^z$ around the black hole and makes an even stronger instability. The code crashes soon after time $t = 12$ when the black hole has only moved slightly. However, in Panel VII, it is shown that the combination of the $\vec{\beta}$ advection term addition and $\tilde{\Gamma}^i$ advection term subtraction, i.e., $\lambda_1 = \lambda_2 = \lambda_4 = 1$, can suppress the unstable modes introduced by the sole usage of these two terms (see Gauges III and V). We can see that the curve profiles of all the variables in Panel VII look almost the same as those in Panel II. It is interesting to note that, according to our literature search, Gauge VII has never been previously used in any BBH simulations. Therefore, it deserves further study. In Panel VIII, we consider the combination of adding the \vec{B} advection term and subtracting the $\tilde{\Gamma}^i$ advection term, i.e., $\lambda_1 = \lambda_3 = \lambda_4 = 1$. The performance in Panel VIII shows a set of curve profiles which are similar to those obtained with Gauge V. Finally, we consider in Panel IX the combination of all three advection terms in the shift equation, i.e., $\lambda_1 = \lambda_2 = \lambda_3 = \lambda_4 = 1$. The combination of the BSSN equations with Gauge IX has been proven to be strongly hyperbolic in the sense of first-order in time, second-order in space systems [37], and thus yields a well-posed initial-value problem. Panel IX shows that all the variables behave very well and smoothly. The curve profiles in Panels II, VII, and IX look almost the same.

The linearized analysis of the BSSN formulation with the gauge conditions in [22] shows that both Gauges II and VII have zero-speed modes. However, from the results described in this section, we can not distinguish the difference between Gauges II, VII and IX. Furthermore, Fig. 5 of [22], which corresponds to gauge II, shows no zero-speed modes at all. We conjecture that the nonlinearity of the full theory could eliminate the zero-speed modes for Gauges II and VII in general. In fact, Gauge II [19, 39], as well as Gauge IX [11, 12, 13], has been successfully used in the simulations of black hole evolution. And Gauge VII is as good as Gauges II and IX for black hole simulations, at least in the cases tested in

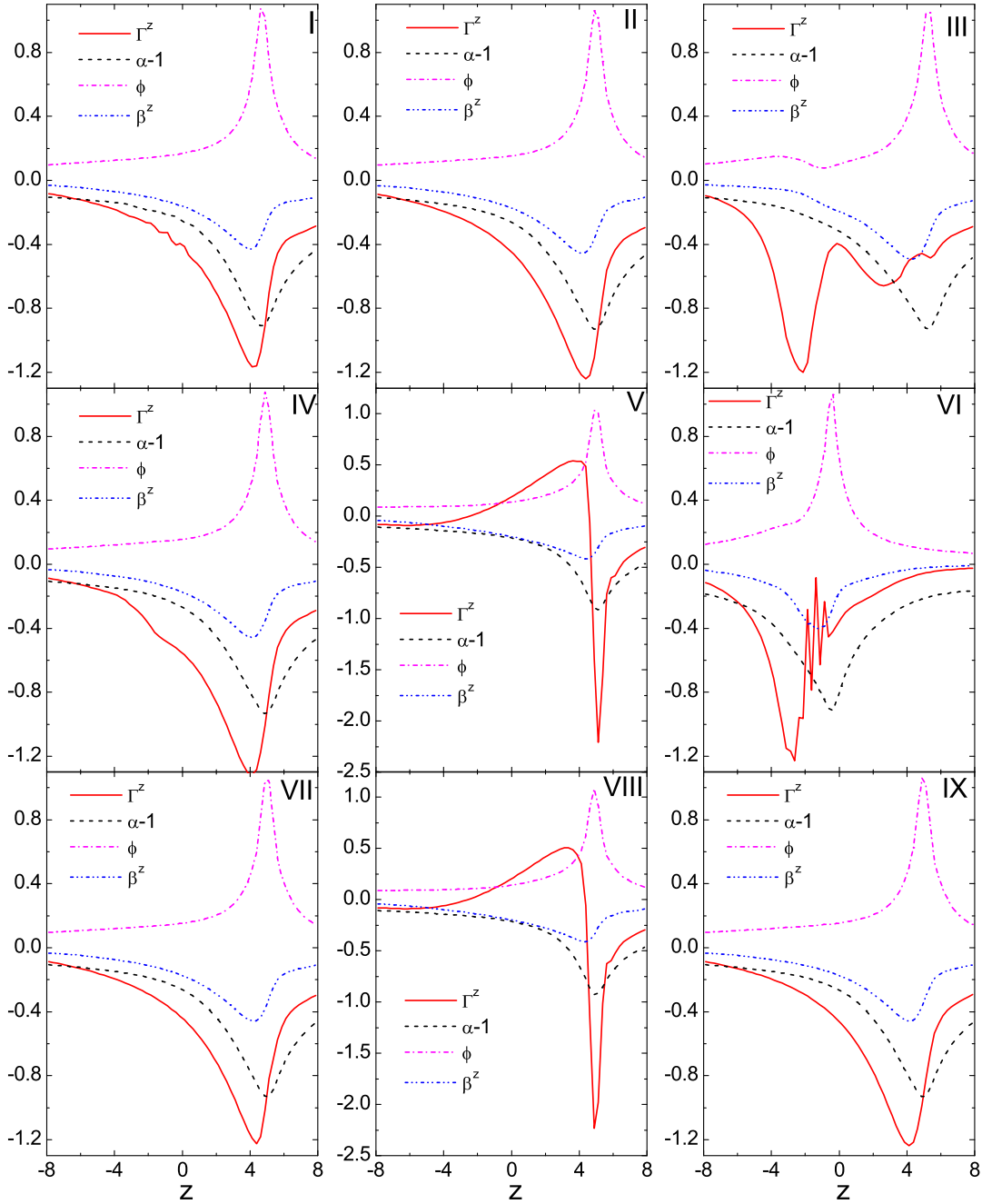


FIG. 3: The gauge tests for a moving black hole without spin (velocity $v \approx 0.615$). The profiles of several dynamical variables at $t = 30$ are shown, except for case VI, for which the time is $t = 12$. The horizontal axis is the z -axis, the moving direction of the black hole. The vertical axis is the corresponding value for different variables: the solid (red) line is Γ^z ; the dashed line is $\alpha - 1$; the (magenta) dot-dashed line is ϕ ; the (blue) dot-dot-dashed line is β^z . The different panels correspond to the different cases in which the gauge number is marked on the upper-right corner of the panel and they are also listed in Table I. For Gauges III, V, and VIII, the results show some ill behavior explicitly while Gauges I and IV have tails of noise behind the black hole. The rest of the three gauge choices II, VII, and IX give almost the same well-behaved result. The results of Gauges II and IX are consistent with other research groups' work. Gauge VII is found to work well with the moving puncture method in this work.

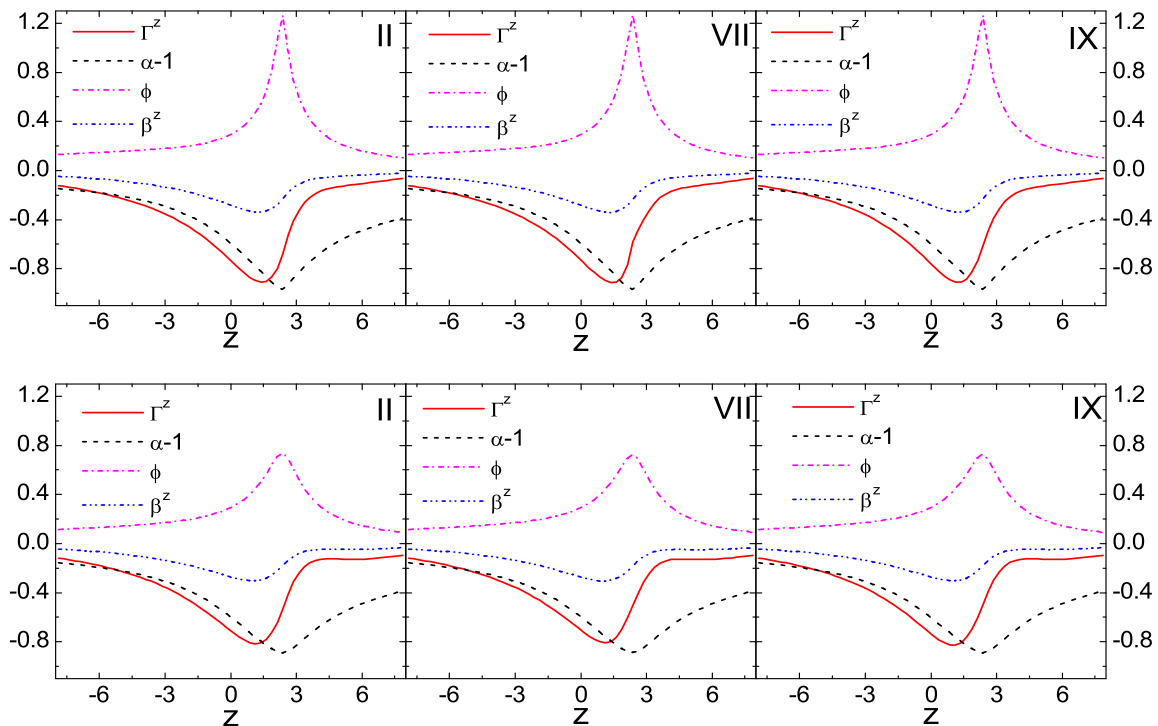


FIG. 4: The gauge tests for a moving black hole with spin parallel (upper panel) and perpendicular (lower panel) to the moving direction (velocity $v \approx 0.5$, the specific angular momentum $a \approx 0.5102$). The profiles of several dynamical variables at $t = 30$ are shown as in Fig. 3. From left to right, the figures correspond to the results with Gauges II, VII and IX listed in Table I, respectively. These three “good” gauges give almost the same results.

this work. Therefore, we can also expect that Gauge VII is very likely to be viable in the generic cases of BBH evolution.

Someone may raise the doubt that the moving velocity is not large enough to excite the zero speed mode for the newly found gauge condition here. This is not the case in fact, at least for the approximate initial data. Considering the ADM mass (34), we have the maximal moving velocity $\vec{v} = \vec{P}_{\text{ADM}}/M_{\text{ADM}}$ for a black hole without spin when $P = 2\sqrt{10}/5$. And the moving velocity ($v \approx 0.615$) for the above tested moving black hole with the linear momentum $P = 1$ almost equals this maximal velocity ($v \approx 0.63$). We have tested this maximal moving velocity also. The result gives the same conclusion mentioned above. Someone may also raise the doubt that the zero speed modes for Gauge VII mentioned in [22] might not be excited in this tested scenario. Therefore, we test it further, with both the case of a moving black hole with spin and the case of a high-spin black hole, in the following subsections. Our results will show that Gauge VII, as well as Gauges II and IX, passes these two tests.

C. Moving Black Hole with Spin

In this subsection, we investigate the effect of spin on a moving black hole. Firstly, we set the spin direction of the black hole to be parallel to its moving direction, specifically, $\vec{P} = (0, 0, 1)$ and $\vec{S} = (0, 0, 1)$. Therefore, the only difference between the setting here and in the previous subsection is that, in this subsection, the black hole has a spin of amplitude 1 which is along the moving direction. Here we only test the “good” gauge choices, i.e., Gauges II, VII and IX. The curve profiles at $t = 30$ are presented in the upper panels of Fig. 4. We find that, with any of these three gauges, the code can stably simulate a spinning black hole. The curves in the three upper panels look the same, not showing a sign of instability. Compared with Fig. 3, we find that the black holes in this case move slower ($v \approx 0.5$) than the spinless ones ($v \approx 0.615$) with the same gauge choices described in the previous subsection. This is consistent with the theoretical prediction: From Eq. (34) we can see that the moving black hole with a nonvanishing spin will have a larger ADM mass than the spinless one due

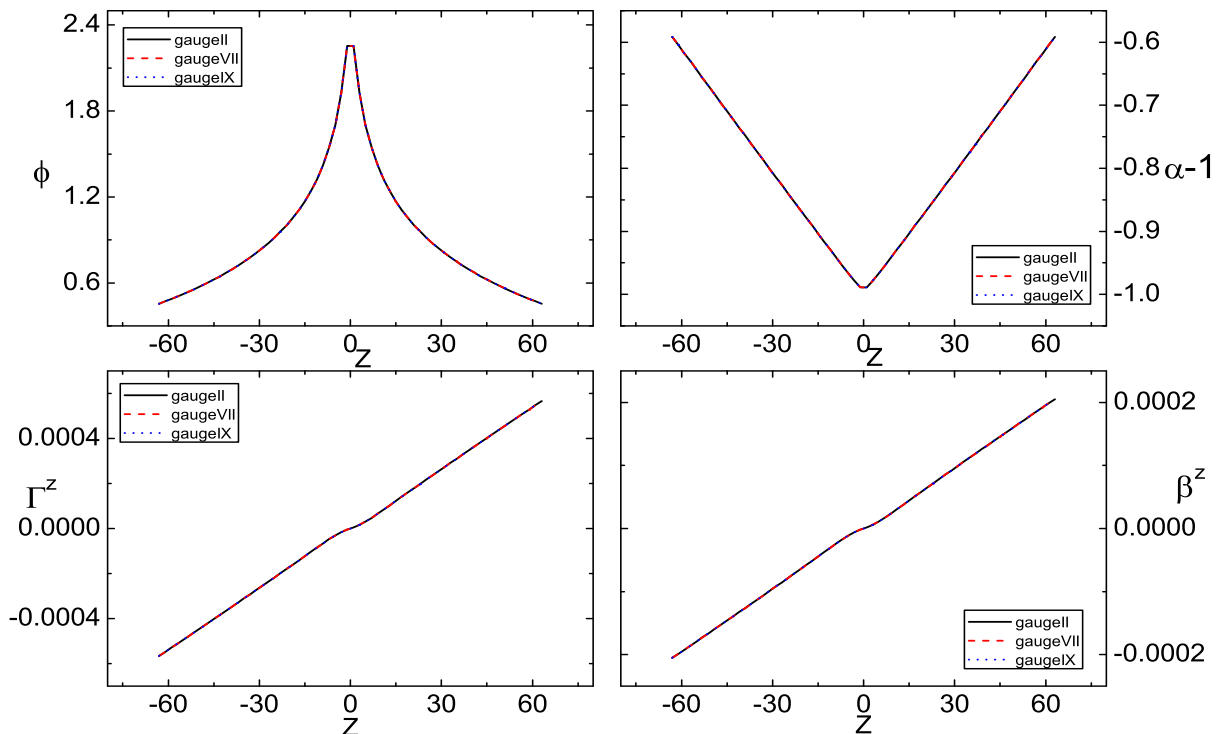


FIG. 5: The gauge tests for a single rapid-rotating black hole (spin parameter $a \approx 0.9$). The comparison of profiles of the three “good” gauges at $t = 30$ is shown. From top to bottom, and from left to right, the panels show the conformal factor ϕ , the lapse $\alpha - 1$, the conformal connection $\tilde{\Gamma}^z$ and the shift β^z , respectively. These three gauge choices give almost the same results.

to the rotational energy. For the moving velocity being $\vec{v} = \vec{P}_{\text{ADM}}/M_{\text{ADM}}$, a spinning black hole will move slower than a spinless one with the same linear momentum. Our conclusion in this test is that Gauges II, VII and IX all handle this scenario well, since these three gauges give almost the same result.

Secondly, we set the spin direction of the black hole to be perpendicular to the moving direction, specifically, $\vec{P} = (0, 0, 1)$ and $\vec{S} = (1, 0, 0)$. Similarly, we only test Gauges II, VII and IX. The curve profiles at $t = 30$ are presented in the lower panels of Fig. 4. The results are similar to those obtained in the parallel-spin case. From Eq. (34), the moving velocity of the black hole for this case is the same as the velocity in the parallel-spin case, i.e., $v \approx 0.5$. We can read this from the results presented in Fig. 4. In this case, the peak amplitude of the variable ϕ becomes smaller than in the parallel-spin case. However, this difference basically comes from the spin orientation; it does not bring any instability to the results with the three “good” gauges II, VII and IX. These three “good” gauges give essentially the same stable behavior.

Similar to the moving velocity being bounded, the magnitude of the specific angular momentum, $\vec{a} =$

\vec{S}/M_{ADM}^2 , has a maximal value for the approximate initial data (32). For $S = \sqrt{5/6}$, the black hole has a maximal magnitude $a = 3\sqrt{30}/32 \approx 0.5135$. The magnitude of \vec{a} in both the parallel-spin and perpendicular-spin cases is $a \approx 0.5102$. Therefore, the magnitude of \vec{a} in these two cases is very close to the maximal magnitude of the specific angular momentum that the initial data can have. In the next subsection we would like to test these three gauge choices with an even higher spin magnitude of \vec{a} .

D. Rapidly-rotating black hole

We have tested Gauge VII in the spinless and the spinning moving black hole cases. We find that, with this gauge choice, the code can simulate these dynamical spacetimes well. Since experience tells us that a higher spin is more likely to trigger a quicker instability in the numerical simulations, one might doubt whether the newly found gauge condition can handle a high-spin case well. In this subsection, we test the three “good” gauge choices with a rapidly-rotating black hole. The ini-

tial data used is another approximate analytic solution for the Bowen-York initial data. We describe the details in Appendix A. This initial data is similar to that used in Sec. V C, except that the conformal factor ψ is given by Eq. (37) rather than Eq. (32) [36, 40] and $\vec{P} = 0$.

Here we set the angular momentum vector to be $\vec{S} = (0, 0, 10000)$, which results in the specific angular momentum $a \approx 0.9$ [36]. In this case, we again only care about the corresponding behavior of the runs with the three “good” gauge choices. The outer boundary is set at $r = 128$, and six levels of grids for FMR are used in the runs. The curve profiles at $t = 30$ are presented in Fig. 5. These three “good” gauge choices can all give a stable and accurate simulation for this highly spinning single black hole case. Looking at the plots in this figure, it is difficult to distinguish between the results obtained with these three gauges. The curves overlap each other well. The profiles of $\tilde{\Gamma}^z$ and β^z are consistent with the experience that they almost give the same shape. Due to the limits on computational resources, the runs are stopped at $t = 30$. This might raise the doubt whether the runtime is long enough to excite an unstable mode. Since the spin of the black hole in this case is close to the maximal one ($a_{\max} \approx 0.9282$) that a punctured black hole can have in a Bowen-York type initial data [36], we expect that some difference between these runs, caused from instability, will appear in this period of time. However, we find that the results with these three gauge choices are almost the same. This should indicate that Gauge VII is as good as the other two in this case, unless all three of these gauge choices cause the same instability, which is highly unlikely. Meanwhile, the results in Sec. V A can be regarded as complementary to the one in this subsection (about the the long-term stability issue of Gauge VII). Therefore we conclude that the new gauge choice, Gauge VII, survives in this high-spin test.

E. Head-on Collision of two equal mass black holes

In the previous subsections, we have presented the numerical simulations for a single black hole with/without spin with the different gauge choices. In order to test our code as well as the three gauge choices discussed above further, we present in this and the next subsections the numerical results about the head-on collisions of a BBH system, which is the simplest case for BBHs. We use time-symmetric initial data for the two black holes, i.e., the so-called Brill-Lindquist initial data [41]. Specifically, the initial data takes the form

$$e^\phi = 1 + \frac{m_1}{2|\vec{r} - \vec{c}_1|} + \frac{m_2}{2|\vec{r} - \vec{c}_2|}, \quad (41)$$

$$\tilde{\gamma}_{ij} = f_{ij}, \quad K = 0, \quad \tilde{A}_{ij} = 0. \quad (42)$$

where m_1 and m_2 are the mass parameters for the two black holes, \vec{c}_1 and \vec{c}_2 are the positions of the black holes, and f_{ij} stands for the flat three-metric. In this case,

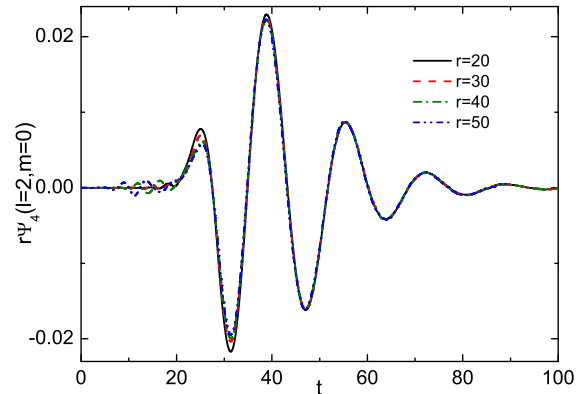


FIG. 6: The $(\ell=2, m=0)$ mode of $r\Psi_4$ extracted from a head-on collision of the Brill-Lindquist initial data starting from the approximate ISCO separation $d = 2.303$ at four different radii $r=20, 30, 40$ and 50 . Considering the velocity of the gravitational wave, the time delay has been shifted in the plot.

we set the mass parameters to be $m_1 = m_2 = 0.5$ and the positions of the two black holes at $(0, 0, \pm 1.1515)$, respectively. This value has been used in [13, 42, 43] and corresponds to an initial separation of the black holes equal to that of an approximate ISCO configuration. In other words, our initial data corresponds to two identical black holes which have no spin and no linear momentum, attracting each other from rest at the ISCO.

In this and the next subsections, the computational domain is $\pm 64 \times \pm 64 \times 64$ and $64 \times 64 \times 32$ grid points are used in every level. To reduce the computational load equatorial symmetry is assumed. Six levels of grids are used for the mesh refinement. The refinement boundaries are placed at 32, 16, 8, 4, and 2. As mentioned in Sec. II B, the χ -version of the evolution equations are also available in our code. In this and the next subsections, we test both the ϕ -version and the χ -version of the code in the head-on collision cases. The results obtained from these two versions are consistent in the scenarios [55].

Although conceptually simple, the head-on collision of a BBH system is still a highly dynamical process in spacetime. During the collision, the system will emit a complete gravitational waveform from the merger of two black holes. To quantify the gravitational waveform, we use the Newman-Penrose scalar Ψ_4 . The method of computing this quantity is described in Appendix B. Due to the symmetric property of this BBH system, the gravitational wave has only the $(\ell=2, m=0)$ mode. First, we consider Gauge IX, which has been widely adopted in simulations of BBH systems. We extract the waveform at $r=20, 30, 40$, and 50 . Since the leading order of Ψ_4 is $1/r$ asymptotically, $r\Psi_4$ should be independent of the extraction position, except for the time delay due to the

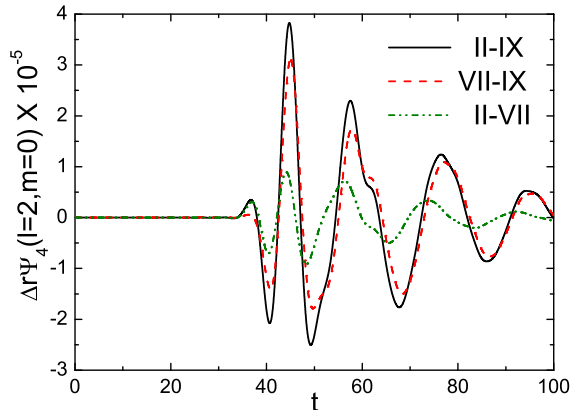


FIG. 7: The differences between the $(\ell=2, m=0)$ mode of the waveform $r\Psi_4$ for different gauge choices extracted at $r = 30$. The solid line is the difference between Gauges II and IX, the (red) dashed line is the difference between Gauges VII and IX, and the (olive) dot-dot-dashed line is the difference between Gauges II and VII. The largest difference is roughly 0.2% of the amplitude of $r\Psi_4$.

gravitational wave propagation. We consider the velocity of the gravitational wave to be the speed of light and thus subtract the time delay accordingly. The waveforms are plotted in Fig. 6. The result is quantitatively consistent [56] with the result reported in [13, 44]. Initially there seems to be some small amplitude oscillations before the larger oscillations for the monitors at larger radii r , but not for the one at smaller r . This noise mainly comes from the reduced accuracy of the evolution in the coarser grids.

We next study the effect of the gauge conditions discussed in the previous subsections in the head-on collision. The differences of the waveforms with the gauge choices are shown in Fig. 7. As expected, the codes with these three “good” gauge conditions can all evolve the head-on collision process stably. However, the gauge conditions indeed affect the waveform [45]. The highest peak of the difference between Gauges II and IX, $\Delta(r\Psi_4)_{\text{II-IX}}$, is about 4×10^{-5} . From the plot, we can see that the pattern and the amplitude of $\Delta(r\Psi_4)_{\text{VII-IX}}$, the (red) dashed line, is close to $\Delta(r\Psi_4)_{\text{II-IX}}$, the solid line. The amplitude of the wave is about 0.02, so the relative difference is about 0.2% of the amplitude of $r\Psi_4$. But it is interesting to note that the amplitude of $\Delta(r\Psi_4)_{\text{II-VII}}$, the (green) dot-dashed line, is smaller, only about 0.05%. We note that these differences are smaller than the difference of wave form resulting from the different initial lapse profile (for example $\alpha = 1, 1/\psi^2, 1/\psi^4$, etc.) which is typically 1% of the amplitude of $r\Psi_4$.

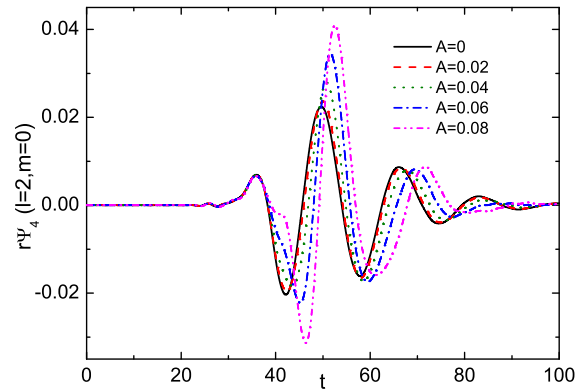


FIG. 8: The $(\ell=2, m=0)$ mode of the waveform $r\Psi_4$ for a massless scalar field perturbing the head-on collision of two identical black holes without spin or linear momentum. A is the strength of the perturbation. $A = 0.0$ means without perturbation. The extraction radius is $r = 30$. The time delay effect of the perturbation is clear. The perturbation will efficiently amplify the waveform.

F. Head-on Collision Perturbed by a Massless Scalar Field

In the previous case, we studied the head-on collision of a BBH system without matter. However, matter is attracted into strong gravitational systems. Thus matter also plays an important role in binary compact objects. The evolution of a dynamic spacetime generally needs to include matter. On the other hand, most of the astrophysical systems, including BBH mergers, are usually surrounded by an accretion disk or some kind of matter. Therefore, it is interesting to ask how this matter will affect the gravitational wave signal, which is expected to be detected in the near future. In order to check the consistency with the matter coupling in the code and to investigate the effect on the gravitational waveform by matter, we study the head-on collision “perturbed” by a scalar field in this subsection. Here “perturbed” means that the amplitude of the scalar field is small, and we do not need to solve the constraint equation to get exact initial data. Instead, we set the dynamical variables of geometry to be identical to those in the previous subsection. Furthermore, the matter part of the dynamical variables are set independently. However when we evolve this initial data, we do not do any approximation, that is to say we solve the fully coupled Einstein-Klein-Golden equation numerically.

The evolution equation of a scalar field is described in Appendix D. For each simulation, we provide the following initial data for Φ and $\partial_t\Phi$: the profiles of Φ are a rest sphere shaped scalar field located at the center of the two

black holes

$$\Phi(t=0) = Ae^{-r^2}, \quad \partial_t \Phi(t=0) = 0, \quad (43)$$

where A is the amplitude of the scalar field. We test the scalar field with different amplitudes to see its effect on the waveform. The amplitudes are set to be $A=0.02, 0.04, 0.06,$ and 0.08 . The results are plotted in Fig. 8. It is clear to see that the waveform is delayed with the existence of the scalar field, and the larger the amplitude of the scalar field is, the longer the delay time. In the meantime, the amplitude of the waveform also becomes larger. This phenomenon can be understood as follows: The scalar field is located at the middle of the black hole. Some part of the scalar field will escape outwards when it evolves. This escaping part of the scalar field will delay the motion of the two black holes toward each other. Meanwhile, some part of the scalar field will be absorbed into the black holes. Thus, the black holes will become larger, and this results in a larger amplitude of the gravitational waveform.

VI. SUMMARY

In summary, we have constructed from scratch a new numerical code based on the BSSN formalism and the moving puncture technique. In the code, an FMR/AMR algorithm is implemented via the GrACE package, a fourth-order spatial finite-differencing scheme and an iterative Crank-Nicholson scheme for time integrations are applied in solving the Einstein equations. Some adjustments of the BSSN formulation for the constraint equations in [26] are also examined in the work. We have compared the alternative adjustments with the conventional ones with a static Schwarzschild black hole and found that with both of them the black hole can be evolved stably and accurately. We then investigated the viability of several gauge choices through the simulation of a single moving black hole with and without spin. In addition to obtaining results consistent with those of other researchers, we found a new gauge choice with which one can also simulate a moving punctured black hole well. We next tested our code with the head-on collisions of a BBH system in a vacuum and with the perturbation of a massless scalar field. The gravitational waveform obtained in this code from the collision in vacuum is quantitatively the same as that obtained in the work by other groups. The purpose of the head-on collision perturbed by a scalar field is to understand qualitatively the effect of matter on the evolution of binary black holes, as well as testing the code further. The result shows that, with a specific configuration, the existence of a scalar field could delay the merger of binary black holes, as people have expected. The strength of the scalar field will significantly affect the gravitational waveform.

The main goal of this work is the construction of a new code for the study of numerical relativity. However, re-investigating the conventional methods and exploring the

alternatives to the methods are also emphasized during the development of this code. As one can see in Sec. V A, both adjustments for the constraint equations give stable and convergent results. However, Fig. 2 also gives the impression that the alternate adjustment performs better than the conventional adjustment. This simply indicates that there is still an issue of the optimal choice of the constraint addition in the Einstein equations. For the gauge condition, our study shows that a new gauge choice, i.e., Gauge VII, is able to pass all of our tests. Therefore, this gauge could be a possible choice for BBH simulations, although more investigation is needed. The waveform obtained from the head-on collisions shows that with the code one can simulate the evolution of a BBH system. This enables us not only to continue studying numerical relativity in more complicated scenarios, like the inspiral of binary black holes, the recoil problem, and the final spin problem, but also to verify the existing results and to go even farther. We believe there will never be too much double-checking of existing achievements, and any further investigations based on them. The result of the head-on collision perturbed by a scalar field gives us some insight into the possible distortion of a gravitational wave, since matter is abundant in most of the gravitating systems.

All of these results verify that the code is reliable and ready to be engaged in the study of more realistic, astrophysical scenarios and of numerical relativity. We plan to use this new code to work on the inspiral of BBH systems in the very near future. One black hole can be determined totally by only 2 parameters, i.e., mass and spin. Thus it is interesting to ask how to determine the product black hole of a BBH system from the information of the two initial black holes. The spin expansion method in [46] shows us some hint as to how to solve this problem, and we plan to study this problem with the new code next.

Acknowledgments

We are grateful to Dr. Ronald Taam for helpful discussions and encouragement and also to Dr. Manish Parashar for offering us the GrACE library. This work was supported in part by the National Science Council under the grants NSC95-2112-M-006-017-MY2 and NSC97-2112-M-006-008. Z. Cao is supported in part by the NSFC (Nos. 10671196 and 10731080). This work was also supported in part by the National Center of Theoretical Sciences. We are grateful to the National Center for High-performance Computing for the use of computer time and facilities.

APPENDIX A: THE APPROXIMATE BOWEN-YORK INITIAL DATA

In the puncture method, the Hamiltonian constraint equation of the Bowen-York initial data reduces to Eq. (31). When the linear momentum \vec{P} and the spin \vec{S} of a black hole are small, we can solve the equation approximately as

$$(\partial_x^2 + \partial_y^2 + \partial_z^2)u = -\frac{1}{8}\hat{K}^{ij}\hat{K}_{ij}(1 + \frac{m}{2r})^{-7}. \quad (\text{A1})$$

We chose the coordinates such that \vec{P} points along the z -direction and \vec{S} lies on the xz coordinate plane, i.e., $\vec{S} = (S_x, 0, S_z)$. In spherical coordinates, we have

$$\begin{aligned} P^r &= P \cos \theta, \\ P^\theta &= -P \sin \theta / r, \\ P^\varphi &= 0, \\ S^r &= S_x \cos \varphi \sin \theta + S_z \cos \theta, \\ S^\theta &= (S_x \cos \varphi \cos \theta - S_z \sin \theta) / r, \\ S^\varphi &= -S_x \sin \varphi / r \sin \theta. \end{aligned} \quad (\text{A2})$$

Note that $\epsilon_{r\theta\varphi} = r^2 \sin \theta$ in spherical coordinates. From Eqs. (2) and (30), \hat{K}_{ij} reads

$$\begin{aligned} \hat{K}_{rr} &= \frac{3P}{r^2} \cos \theta, \\ \hat{K}_{r\theta} &= -\frac{3P}{2r} \sin \theta - \frac{3}{r^2} S_x \sin \varphi, \\ \hat{K}_{r\varphi} &= -\frac{3 \sin \theta}{r^2} (S_x \cos \varphi \cos \theta - S_z \sin \theta), \\ \hat{K}_{\theta\theta} &= -\frac{3P}{2} \cos \theta, \\ \hat{K}_{\theta\varphi} &= 0, \\ \hat{K}_{\varphi\varphi} &= -\frac{3P}{2} \cos \theta \sin^2 \theta. \end{aligned} \quad (\text{A3})$$

Then

$$\begin{aligned} \hat{K}^{ij}\hat{K}_{ij} &= \frac{9P^2}{2r^4} \left[\frac{5}{3} + \frac{2}{3}(3 \cos^2 \theta - 1) \right] \\ &+ \frac{9}{r^6} S_x^2 \left[\frac{4}{3} + \frac{1}{3}(3 \cos^2 \theta - 1) - \sin^2 \theta \cos 2\varphi \right] \\ &+ \frac{18S_z^2}{r^6} \left[\frac{2}{3} - \frac{1}{3}(3 \cos^2 \theta - 1) \right] \\ &+ \frac{18}{r^5} P S_x \sin \theta \sin \varphi - \frac{36}{r^6} S_x S_z \cos \theta \sin \theta \sin \varphi. \end{aligned} \quad (\text{A4})$$

By introducing the two new variables, $\mu_P = \vec{P} \cdot \vec{n} / P$ and $\mu_S = \vec{S} \cdot \vec{n} / S$, Eq. (A4) can be rewritten as

$$\begin{aligned} \hat{K}^{ij}\hat{K}_{ij} &= \frac{9P^2}{2r^4} \left[\frac{5}{3} + \frac{2}{3}(3\mu_P^2 - 1) \right] \\ &+ \frac{18S^2}{r^6} \left[\frac{2}{3} - \frac{1}{3}(3\mu_S^2 - 1) \right] + \frac{18}{r^6} (\vec{P} \times \vec{S}) \cdot \vec{r}. \end{aligned} \quad (\text{A5})$$

Since Eq. (31) is mainly linear with respect to u , we can solve it by dividing $\hat{K}^{ij}\hat{K}_{ij}$ into three parts, i.e., the P^2 part, the S^2 part, and the $\vec{P} \times \vec{S}$ part. With a variable separation method, we can get the solution of Eq. (31) [35, 39], i.e., Eq. (32).

For the scenario that $\vec{P} = 0$ while the spin is large, the solution of Eq. (31) can be approximated with the spherical symmetric solution [36]. Then Eq. (31) can be smeared out as

$$(\partial_x^2 + \partial_y^2 + \partial_z^2)\psi = -\frac{3S^2}{2r^6}\psi^{-7}. \quad (\text{A6})$$

In spherical coordinates, this equation reads

$$(\partial_r^2 + \frac{2}{r}\partial_r)\psi = -\frac{3S^2}{2r^6}\psi^{-7}. \quad (\text{A7})$$

Following Dain [40] we assume that ψ behaves according to a power-law ($\psi = Ar^\alpha$) and substitute this into Eq. (A7). We find that the approximate solution for a highly-spinning black hole is

$$\psi = \frac{(6S^2)^{1/8}}{\sqrt{r}}. \quad (\text{A8})$$

However, this approximate solution is valid only for $m^3/S < r < S/m$, which implies that the larger the spin is, the better the approximation is.

APPENDIX B: WAVE EXTRACTION WITH Ψ_4

In our code we use the Newman-Penrose scalar Ψ_4 for extracting the physical information from numerical simulations. Here we follow Pretorius' work [7] and construct the tetrad from the timelike unit normal field as well as applying the Gram-Schmidt orthonormalization procedure to the three-dimensional vectors

$$\begin{aligned} \vec{u} &= [x, y, z], \\ \vec{v} &= [-y, x, 0], \\ \vec{w} &= [xz, yz, -(x^2 + y^2)]. \end{aligned} \quad (\text{B1})$$

The tetrad vectors are then given by [11]

$$\begin{aligned} n^0 &= \frac{1}{\sqrt{2}\alpha}, & n^i &= \frac{1}{\sqrt{2}} \left(\frac{-\beta^i}{\alpha} - u^i \right), \\ \ell^0 &= \frac{1}{\sqrt{2}\alpha}, & \ell^i &= \frac{1}{\sqrt{2}} \left(\frac{-\beta^i}{\alpha} + u^i \right), \\ m^0 &= 0, & m^i &= \frac{1}{\sqrt{2}} (v^i + iw^i). \end{aligned} \quad (\text{B2})$$

From the definition of Ψ_4 and Gauss-Codazzi-Mainardi equations [47, 48], we have

$$\begin{aligned} \Psi_4 &= -{}^{(4)}R_{\alpha\beta\gamma\delta} n^\alpha \bar{m}^\beta n^\gamma \bar{m}^\delta \\ &= -\frac{1}{2} [n^0 n^0 (R_{j\ell} - K_{jp} K_\ell^p + K K_{j\ell}) + 4n^0 n^k D_{[k} K_{\ell]j} \\ &+ n^i n^k (R_{ijk\ell} + 2K_{i[k} K_{\ell]j})] (v^j - iw^j)(v^\ell - iw^\ell) \end{aligned} \quad (\text{B3})$$

All the quantities in the last equation are physical ones in the three-dimensional hypersurface. Let us relate them to the conformal ones

$$\begin{aligned}
R_{ijkl} &= e^{4\phi}(\tilde{R}_{ijkl} + 4\tilde{\gamma}_{\ell[i}\tilde{D}_{j]}\tilde{D}_k\phi - 4\tilde{\gamma}_{k[i}\tilde{D}_{j]}\tilde{D}_\ell\phi \\
&\quad - 16\phi_{,[i}\tilde{\gamma}_{j]k}\phi_{,\ell]} - 8\tilde{\gamma}_{k[i}\tilde{\gamma}_{j]\ell}\tilde{\gamma}^{mn}\phi_{,m}\phi_{,n}), \\
R_{ij} &= \tilde{R}_{ij} - 2\tilde{D}_i\tilde{D}_j\phi - 2\tilde{\gamma}_{ij}\tilde{D}^k\tilde{D}_k\phi + 4\phi_{,i}\phi_{,j} \\
&\quad - 4\tilde{\gamma}_{ij}\tilde{\gamma}^{mn}\phi_{,m}\phi_{,n}, \\
K_{ij} &= e^{4\phi}(\tilde{A}_{ij} + \frac{1}{3}\tilde{\gamma}_{ij}K), \\
D_iK_{jk} &= e^{4\phi}(\tilde{A}_{jk,i} - 2\tilde{\Gamma}^\ell_{i(j}\tilde{A}_{k)\ell} + \frac{1}{3}\tilde{\gamma}_{jk}K_{,i}) \\
&\quad - 4K_{i(j}\phi_{,k)} + 4\tilde{\gamma}_{i(j}K_{k)m}\tilde{\gamma}^{m\ell}\phi_{,\ell}.
\end{aligned} \tag{B4}$$

Combining these equations together, we are able to compute Ψ_4 on the entire three-hypersurface. When we transform m^μ to $e^{i\zeta}m^\mu$, Ψ_4 will be transformed to $e^{-2i\zeta}\Psi_4$ which results from Eq. (B3). The functions with this kind of property are said to have spin weight -2. Since the functions with different spin weight are orthogonal, we can calculate the corresponding coefficients $A_{\ell m}$ with respect to the spin weighted spherical harmonic function with spin weight -2 [11, 49], i.e., $Y_{\ell m}^{-2}$. The major reason for choosing this type of function set is to reduce numerical error during the calculations. The coefficients of the gravitational radiation can be obtained from the integration of Ψ_4 and each $Y_{\ell m}^{-2}$,

$$A_{\ell m} = \langle Y_{\ell m}^{-2}, \Psi_4 \rangle \equiv \int_0^{2\pi} \int_0^\pi \overline{Y_{\ell m}^{-2}} \Psi_4 \sin\theta d\theta d\varphi, \tag{B5}$$

where $\ell \geq 2$ and $-\ell \leq m \leq \ell$. The spin-weighted spherical harmonics $Y_{\ell m}^{-2}$ can be defined in terms of the Wigner d-functions (e.g., [11]) as

$$Y_{\ell m}^{-2}(\theta, \varphi) = \sqrt{\frac{2\ell+1}{4\pi}} d_{m2}^\ell(\theta) e^{im\varphi}, \tag{B6}$$

where

$$\begin{aligned}
d_{m2}^\ell(\theta) &= \sum_{t=C_1}^{C_2} \frac{(-1)^t \sqrt{(\ell+m)!(\ell-m)!}}{(\ell+m-t)!(\ell+2-t)!} \\
&\quad \frac{\sqrt{(\ell-2)!(\ell+2)!}}{(t-2-m)!t!} \left(\cos\frac{\theta}{2}\right)^{2\ell+m+2-2t} \left(\sin\frac{\theta}{2}\right)^{2t-2-m}, \tag{B7}
\end{aligned}$$

with $C_1 = \max(0, m-2)$ and $C_2 = \min(\ell+m, \ell-2)$.

APPENDIX C: THE APPLICATION OF THE UNIMODULAR DETERMINANT CONSTRAINT

In the BSSN formulation the determinant of the conformal metric is unimodular, i.e., Eq. (18). The first spatial derivative of Eq. (18) gives

$$\tilde{\gamma}^{ij}\tilde{\gamma}_{ij,k} = 0 \implies \tilde{\Gamma}^j_{jk} = 0. \tag{C1}$$

We have imposed these three ‘‘secondary’’ constraints in the calculation of the conformal Ricci curvature, \tilde{R}_{ij} and obtain its expression as in Eq. (10). The explicit expression of the scalar curvature \tilde{R} is

$$\tilde{R} = -\frac{1}{2}\tilde{\gamma}^{ij}\tilde{\gamma}^{k\ell}\tilde{\gamma}_{ij,k\ell} + \tilde{\Gamma}^k_{,k} + \tilde{\Gamma}^{ijk} \left(2\tilde{\Gamma}_{jik} + \tilde{\Gamma}_{ijk} \right). \tag{C2}$$

Here the constraints (C1) have been used again.

The second spatial derivative of the unimodular determinant constraint gives

$$\tilde{\gamma}^{k\ell}\tilde{\gamma}_{k\ell,ij} - 4\tilde{\Gamma}_{k\ell i}\tilde{\Gamma}^{(k\ell)}_j = 0, \tag{C3}$$

and the trace of this ‘‘tertiary’’ constraint is

$$\tilde{\gamma}^{ij}\tilde{\gamma}^{k\ell}\tilde{\gamma}_{ij,k\ell} - 4\tilde{\Gamma}_{ijk}\tilde{\Gamma}^{(ij)k} = 0. \tag{C4}$$

Using Eq. (C4) we can rewrite Eq. (C2) to be

$$\tilde{R} = \partial_i\tilde{\Gamma}^i + \tilde{\Gamma}^{ijk}\tilde{\Gamma}_{jik}. \tag{C5}$$

Here the conformal trace curvature is only dependent on the first derivatives of the conformal connection $\tilde{\Gamma}^i$ and of the conformal metric $\tilde{\gamma}_{ij}$.

The modified ADM mass volume integral in [26]

$$\begin{aligned}
M &= \frac{1}{16\pi} \int_\Omega d^3x \left[e^{5\phi} \left(16\pi\rho + \tilde{A}_{ij}\tilde{A}^{ij} - \frac{2}{3}K^2 \right) \right. \\
&\quad \left. - \tilde{\Gamma}^{ijk}\tilde{\Gamma}_{jik} + (1 - e^\phi)\tilde{R} \right], \tag{C6}
\end{aligned}$$

can be understood better now with the expression (C5). Applying Eq. (C5) to Eq. (C6) we have

$$\begin{aligned}
M &= \frac{1}{16\pi} \int_\Omega d^3x \left[e^{5\phi} \left(16\pi\rho + \tilde{A}_{ij}\tilde{A}^{ij} - \frac{2}{3}K^2 \right) \right. \\
&\quad \left. + \partial_i\tilde{\Gamma}^i - e^\phi\tilde{R} \right]. \tag{C7}
\end{aligned}$$

For the cases in which $\tilde{\Gamma}^i$ is negligible, the ADM mass integral expression returns to

$$M = \frac{1}{16\pi} \int_\Omega d^3x \left[e^{5\phi} \left(16\pi\rho + \tilde{A}_{ij}\tilde{A}^{ij} - \frac{2}{3}K^2 \right) - e^\phi\tilde{R} \right] \tag{C8}$$

APPENDIX D: SCALAR FIELD IN A CURVED SPACETIME

The dynamics of a complex scalar field in a curved spacetime is described by the following Lagrangian density [50, 51]

$$\mathcal{L} = -\frac{1}{16\pi}R + \frac{1}{2}[\nabla_\mu\bar{\Phi}\nabla^\mu\Phi + V(|\Phi|^2)], \tag{D1}$$

where R is the scalar curvature, Φ is the scalar field, $\bar{\Phi}$ is its complex conjugate, and $V(|\Phi|^2)$ is the potential

depending on $|\Phi|^2$. Here we consider the case where the potential takes the form $V(|\Phi|^2) = m^2|\Phi|^2$ with m being the mass parameter. The action with the Lagrangian leads to Einstein's equation,

$$R_{\mu\nu} - \frac{1}{2}g_{\mu\nu}R = 8\pi T_{\mu\nu}, \quad (\text{D2})$$

where $R_{\mu\nu}$ is the Ricci tensor and $T_{\mu\nu}$ is the stress-energy tensor defined by

$$T_{\mu\nu} = \nabla_{(\mu}\Phi\nabla_{\nu)}\bar{\Phi} - \frac{1}{2}g_{\mu\nu}[\nabla_{\sigma}\Phi\nabla^{\sigma}\bar{\Phi} + m^2|\Phi|^2]. \quad (\text{D3})$$

The matter source terms in the BSSN formulation are constructed from the stress-energy tensor via the expressions [10]

$$\rho = n_{\mu}n_{\nu}T^{\mu\nu}, \quad (\text{D4})$$

$$s_{ij} = \gamma_{i\mu}\gamma_{j\nu}T^{\mu\nu}, \quad (\text{D5})$$

$$s_i = -\gamma_{i\mu}n_{\nu}T^{\mu\nu}, \quad (\text{D6})$$

$$s = \gamma^{ij}s_{ij}. \quad (\text{D7})$$

The field equation for a *massless* scalar field is

$$\nabla_{\mu}\nabla^{\mu}\Phi = 0, \quad (\text{D8})$$

which can be expanded as

$$\nabla_{\mu}\nabla^{\mu}\Phi = \frac{1}{\sqrt{-g}}\partial_{\mu}(\sqrt{-g}g^{\mu\nu}\partial_{\nu}\Phi) = 0. \quad (\text{D9})$$

With the metric given by

$$ds^2 = -\alpha^2 dt^2 + \gamma_{ij}(dx^i + \beta^i dt)(dx^j + \beta^j dt), \quad (\text{D10})$$

we can re-write the field equation and decompose this second-order equation into two first-order-in-time equations:

$$(\partial_t - \beta^i\partial_i)\Phi = \alpha\Pi, \quad (\text{D11})$$

$$\begin{aligned} (\partial_t - \beta^i\partial_i)\Pi &= e^{-4\phi}\alpha[\tilde{\gamma}^{ij}\Phi_{,ij} - (\tilde{\Gamma}^i - 2\tilde{\gamma}^{ij}\phi_{,i})\Phi_{,j}] \\ &+ e^{-4\phi}\tilde{\gamma}^{ij}\alpha_{,i}\Phi_{,j} + \alpha K\Pi. \end{aligned} \quad (\text{D12})$$

Combining Eqs. (D11), (D12) with Einstein's equation, we can study the dynamical interaction between a massless scalar field and the curved space-time where the scalar field lives via the numerical analysis.

-
- [1] B. Berger, Living Rev. Relativity **5**, 1 (2002).
[2] A. Abramovici *et al.*, Science **256**, 325 (1992).
[3] B. Caron *et al.*, Class. Quant. Grav., **14**, 1461 (1997).
[4] H. Lüch, Class. Quant. Grav., **14**, 1471 (1997).
[5] M. Ando *et al.*, Phys. Rev. Lett. **86**, 3950 (2001).
[6] K. Danzmann *et al.*, Pre-Phase A report, 2nd ed. (1998).
[7] F. Pretorius, Phys. Rev. Lett. **95**, 121101 (2005).
[8] M. Campanelli, *et al.*, Phys. Rev. Lett. **96**, 111101 (2006).
[9] J.G. Baker, *et al.*, Phys. Rev. Lett. **96**, 111102 (2006).
[10] T. Nakamura, K. Oohara, and Y. Kojima, Prog. Theor. Phys. Suppl. **90**, 1 (1987); M. Shibata and T. Nakamura, Phys. Rev. D **52**, 5428 (1995); T.W. Baumgarte and S.L. Shapiro, Phys. Rev. D **59**, 024007 (1999).
[11] B. Brügmann, J. Gonzalez, M. Hannam, S. Husa, U. Sperhake and W. Tichy, Phys. Rev. D **77**, 024027 (2008).
[12] B. Vaishnav, I. Hinder, F. Herrmann and D. Shoemaker, Phys. Rev. D **76**, 084020 (2007).
[13] U. Sperhake, Phys. Rev. D **76**, 104015 (2007).
[14] K. Taniguchi, T. Baumgarte, J. Faber, and S. Shapiro, Phys. Rev. D **77**, 044003 (2008); L. Baiotti, B. Giacomazzo, and L. Rezzolla, Phys. Rev. D **78**, 084033 (2008).
[15] J. Baker, M. Campanelli, F. Pretorius, and Y. Zlochower, Class. Quantum Grav. **24**, S25 (2007); J. Baker, S. McWilliams, J. van Meter, J. Centrella, D. Choi, B. Kelly, and M. Koppitz, Phys. Rev. D **75**, 124024 (2007); M. Hannam, S. Husa, J. Gonzalez, U. Sperhake, and B. Brügmann, Phys. Rev. D **77**, 044020 (2008).
[16] J. Baker, J. van Meter, S. McWilliams, J. Centrella, and B. Kelly, Phys. Rev. Lett. **99**, 181101 (2007).
[17] M. Campanelli, C. Lousto, and Y. Zlochower, Phys. Rev. D **74**, 041501(R) (2006); M. Campanelli, C. Lousto, and Y. Zlochower, Phys. Rev. D **74**, 084023 (2006); M. Campanelli, C. Lousto, Y. Zlochower, B. Krishnan, and D. Merritt, Phys. Rev. D **75**, 064030 (2007).
[18] M. Campanelli, Class. Quant. Grav. **22**, S387 (2005); J. Gonzalez, U. Sperhake, B. Brügmann, M. Hannam, and S. Husa, Phys. Rev. Lett. **98**, 231101 (2007); J. Baker, J. Centrella, D. Choi, M. Koppitz, J. van Meter, and M. Miller, The Astrophysical Journal Letters **653** L93 (2006); F. Herrmann, I. Hinder, D. Shoemaker, and P. Laguna, The Astrophysical Journal **661** 430 (2007).
[19] M. Campanelli, C. Lousto, Y. Zlochower, and D. Merritt, Phys. Rev. Lett. **98**, 231102 (2007).
[20] M. Hannam, *et al.*, Phys. Rev. Lett. **99**, 241102 (2006); M. Hannam, *et al.*, J. Phys.: Conf. Ser. **66**, 012047 (2007); T.W. Baumgarte and S.G. Naculich, Phys. Rev. D **75**, 067502 (2007).
[21] C. Bona, J. Masso, E. Seidel and J. Stela, Phys. Rev. Lett. **75**, 600 (1995).
[22] J. Meter, J. Baker, M. Koppitz and, D. Choi, Phys. Rev. D **73**, 124011 (2006).
[23] J. Balakrishna, G. Daues, E. Seidel, W. Suen, M. Tobias, E. Wang, Class. Quantum Grav. **13**, L135 (1996).
[24] M. Parashar, GrACE—Grid Adaptive Computation Engine, <http://www.caip.rutgers.edu/TASSL/Projects/GrACE>.
[25] T.W. Baumgarte and S.L. Shapiro, Phys. Rept. **376**, 41 (2003).
[26] H.J. Yo, T.W. Baumgarte, and S.L. Shapiro, Phys. Rev. D **66**, 084026 (2001).
[27] B. Brügmann, J. A. Gonzalez, M. Hannam, S. Husa, U. Sperhake, and W. Tichy, Phys. Rev. D **77**, 024027 (2008).

- [28] P. Marronetti, W. Tichy, B. Brügmann, J. A. Gonza'lez, U. Sperhake, Phys. Rev. D **77**, 064010 (2008).
- [29] Y. Zlochower, J. Baker, M. Campanelli, and C. Lousto, Phys. Rev. D **72**, 024021 (2005).
- [30] Teukolsky, Phys. Rev. D **61**, 087501 (2000).
- [31] H.O. Kreiss and J. Olinger, *Methods for Approximate Solution of time Dependent Problems* (GARP Publication Series, Geneva, 1973).
- [32] M. Berger and J. Olinger, J. Comp. Phys. **53**, 484(1984).
- [33] B. Imbiriba, J. Baker, D. Choi, J. Centrella, D. Fiske, J. Brown, J. van meter, and K. Olson, Phys. Rev. D **70**, 124025 (2004).
- [34] S. Brandt and B. Brügmann, Phys. Rev. Lett. **78**, 3606 (1997).
- [35] R.J. Gleiser, C.O. Nicasio, R.H. Price, and J. Pullin, Phys. Rev. D **57**, 3401 (1998); R.J. Gleiser, G. Khanna, and J. Pullin, Phys. Rev. D **66**, 024035 (2002); P. Laguna, Phys. Rev. D **69**, 104020 (2004); K. Dennison, T. Baumgarte, and H. Pfeiffer, Phys. Rev. D **74**, 064016 (2006).
- [36] G. Lovelace, R. Owen, H. Pfeiffer, and T. Chu, Phys. Rev. D **78**, 084017 (2008).
- [37] C. Gundlach and J. Martin-Garcia, Phys. Rev. D **74**, 024016 (2006).
- [38] H. Beyer and O. Sarbach, Phys. Rev. D **70**, 104004 (2004).
- [39] C. Lousto and Y. Zlochower, Phys. Rev. D **77**, 024034 (2008).
- [40] S. Dain, C. Lousto, and Y. Zlochower, Phys. Rev. D **78**, 024039 (2008).
- [41] D.R. Brill and R.W. Lindquist, Phys. Rev. **131**, 471 (1964).
- [42] M. Alcubierre, B. Brügmann, P. Diener, M. Koppitz, D. Pollney, E. Seidel, and R. Takahashi, Phys. Rev. D **67**, 084023 (2003).
- [43] G.B. Cook, Phys. Rev. D **50** 5025 (1994); T.W. Baumgarte, Phys. Rev. D **62**, 024018 (2000).
- [44] D. Fiske, J. Baker, J. van Meter, D. Choi, and J. Centrella, Phys. Rev. D **71**, 104036 (2005).
- [45] D. Brown, P. Diener, O. Sarbarch, E. Schnetter, and M. Tiglio, arXiv:0809.3533.
- [46] L. Boyel, M. Kesden, and S. Nissanke, Phys. Rev. Lett., **100**, 151101 (2008); L. Boyel and M. Kesden, Phys. Rev. D, **78**, 024017 (2008).
- [47] M. Campanelli, and C. Lousto, Phys. Rev. D **58**, 024015 (1998).
- [48] J. Baker, M. Campanelli, and C. Lousto, Phys. Rev. D **65**, 044001 (2002).
- [49] X. Wu, Y. Shang, Class. Quantum Grav. **24**, 679 (2007).
- [50] A. Das, J. Math. Phys. **4**, 45 (1963).
- [51] C. Palenzuela, I. Olabarrieta, L. Lehner, S. Liebling, Phys. Rev. D **75**, 064005(2007).
- [52] T. Yamamoto, M. Shibata, and K. Taniguchi, Phys. Rev. D **78**, 064054 (2008).
- [53] It is also pointed out in [28] that W can make the numerical computation near the black hole more accurate than both χ and ϕ . It is shown in [52] that W is more convenient than ϕ to compute the Ricci tensor since $R_{ij} = \tilde{R}_{ij} + R_{ij}^W$ with $R_{ij}^W = \tilde{D}_i \tilde{D}_j W/W + \tilde{\gamma}_{ij}(\tilde{D}_k \tilde{D}^k W/W - 2\tilde{D}_k W \tilde{D}^k W/W^2)$, which is formally simpler than Eq. (11).
- [54] Sometimes we find that it is less accurate if the last step is fulfilled, especially in the higher-order finite-differencing scheme. We then simply neglect the last step in the interface treatment for better accuracy.
- [55] In this work, we mainly stick to the ϕ -version of the code. However, in our experience, the χ -version of the code sometimes gives better stability and convergence, although it also suffers from a possible problem during the evolution, due to χ 's turning negative near the punctures.
- [56] Note the difference of the tetrad by a factor of two between our setting and the setting in [44]. This results in the difference in the magnitude of the waveform by a factor of two.